Potential vorticity: Measuring consistency between GCM dynamical cores and tracer advection schemes†

J. P. Whitehead[a,b*], C. Jablonowski[b], J. Kent[b], and R. B. Rood[b]

[a] *Mathematics Department, Brigham Young University, 350 TMCB, Provo, UT 84602, USA*

[b] *University of Michigan, Department of Atmospheric, Oceanic & Space Sciences, 2455 Hayward St., Ann Arbor, MI 48109, USA*

*Correspondence to: J. P. Whitehead, Mathematics Department, Brigham Young University, 275 TMCB, Provo, UT 84602, USA. E-mail: whitehead@math.byu.edu

Ertel's potential vorticity (PV) is used as a diagnostic tool to give a direct comparison between the treatment of PV in the dynamics and the integration of PV as a passive tracer, yielding a systematic evaluation of a model's consistency between the dynamical core's integration of the equations of motion and its tracer transport algorithm. Several quantitative and qualitative metrics are considered to measure the consistency including error norms and grid-independent probability density functions. Comparisons between the four dynamical cores of the National Center for Atmospheric Research's (NCAR) Community Atmosphere Model version 5.1 (CAM) are presented.

We investigate the consistency of these dynamical cores in an idealized setting; the presence of a breaking baroclinic wave. For linear flow, before the wave breaks, the consistency for each model is good. As the flow becomes nonlinear the consistency between dynamic PV and tracer PV breaks down, especially at small scales. Large values of dynamic PV are observed that do not appear in the tracer PV. The results indicate that the spectral-element (CAM-SE) dynamical core is the most consistent of the dynamical cores in CAM, however, the consistency between dynamic PV and tracer PV is related to and sensitive to the diffusive properties of the dynamical cores.

Key Words: dynamical core, tracer transport, potential vorticity, advection, test case, baroclinic wave

Received . . .

Citation: . . .

1. Introduction

Much attention has been paid of late to the evaluation and accuracy of the dynamical cores of general circulation models (GCM). The term dynamical core refers to the integration of the nonlinear equations of motion and typically includes all transport processes. One of the key building blocks for a dynamical core is the advection scheme that passively advects the many, possibly hundreds of tracers used in climate studies (Lamarque *et al.* 2008). Tracer advection schemes implicitly rely on the accurate integration of the momentum equation because the advective winds are taken from this dynamic step. Some models even use the identical tracer advection algorithm as a building block for integrating both the tracers and the momentum equations (Lin 2004; Lin and Rood 1996). Tracer advection routines and the integration of the nonlinear dynamics are therefore fundamentally linked. The impact that this relationship has on the subgrid (unresolved) scales needs further quantification. The current paper is one approach to this problem.

Investigations into the veracity of a model's tracer transport algorithm (see Lauritzen *et al.* (2011)) are necessary to validate model performance. Typically, such test

cases are performed on a variety of modeling frameworks, isolating the effect of the advective transport via a series of tests with variable difficulty (Kent *et al.* 2012a; Nair and Lauritzen 2010). These tests have prescribed dynamical fields, such as prescribed wind velocities, and omit the parameterized physics, concentrating on the advection algorithm. Other tests such as the adiabatic baroclinic wave test by Jablonowski and Williamson (2006a) provide a means to compare the evolution of the nonlinear dynamics (as opposed to the linear tracer advection equation) between models, while omitting the effect of complicated physics parameterizations. In a different approach to examining the dynamical core or tracer advection routine separately, Rasch *et al.* (2006) closely monitored the effect of different tracer routines on climate related constituents, using the full physics parameterization package available in the National Center for Atmospheric Research (NCAR)'s Community Atmosphere Model (CAM) version 3.0. Rasch *et al.* (2006) considered three of the dynamical cores available in CAM. These are named after the discretization method of the prognostic equations in the dynamical core: finite volume (CAM-FV), spectral-transform Eulerian (CAM-EUL), and spectral-transform semi-Lagrangian (CAM-SLD). They found that even with the identical physics parameterization package, the evolution of the tracers depended on the choice of dynamical core and hence the choice of the advection algorithm. By investigating the relationship between the discrete integration of the dynamics and the corresponding tracer transport algorithm within each of the four dynamical cores in CAM version 5.1 (Neale *et al.* 2010), we shed some light on the results of Rasch *et al.* (2006).

In Williamson (2007) it is noted that employing two different numerical schemes for the integration of the dynamics and for tracer advection "is not entirely satisfactory". This aspect is, for example, illustrated in Zhang *et al.* (2008). They observed that a tracer advection scheme that was not inherently consistent with the dynamical framework in the atmospheric model GAMIL (Wang *et al.* 2004; Wan *et al.* 2006) led to significant errors in a radon transport test. Adjusting the advective scheme appropriately appeared to reduce the impact of these errors, and Zhang *et al.* (2008) proposed that the difference arose from the lack of consistency of the originally-used advective scheme. These results highlight only some of the possible issues that may arise from treating advection differently than the dynamics (Lee *et al.* 2004; Lauritzen *et al.* 2011). Furthermore, Joeckel *et al.* (2001) emphasized these ideas, arguing that for accurate constituent transport, the discrete advective continuity equation should reduce to that used for the transport of mass (dynamics). This restriction on the design of a dynamical core was one of the primary considerations in the design of CAM-FV (Rood 2011; Lin 2004; Lin and Rood 1996). In this paper we suggest an idealized approach that measures this "consistency" between the dynamical core and its tracer advection scheme. This is done via the assessment of Ertel's potential vorticity that acts both as a dynamic quantity and passive tracer.

Ertel's potential vorticity (PV) with symbol q is defined as

$$q = \frac{1}{\rho}(2\boldsymbol{\Omega} + \nabla \times \boldsymbol{u}) \cdot (\nabla\theta), \tag{1}$$

where ρ is the density of the air, $\boldsymbol{u}$ stands for the three-dimensional velocity vector field, $\boldsymbol{\Omega}$ symbolizes the Earth's rotation vector, θ denotes the potential temperature, and $\nabla\times$ and ∇ are the curl and gradient operators. When the hydrostatic and shallow-atmosphere approximations are made, as is the case for the hydrostatic primitive equations, then the isobaric and isentropic versions of Eq. (1) are

$$q = -g(f\hat{\boldsymbol{k}} + \nabla_p \times \boldsymbol{v}) \cdot \nabla_p\theta \tag{2}$$

$$q = -g(f + \hat{\boldsymbol{k}} \cdot \nabla_\theta \times \boldsymbol{v})\frac{\partial\theta}{\partial p}, \tag{3}$$

respectively (Hoskins *et al.* 1985). Here, g symbolizes the gravity, $\hat{\boldsymbol{k}}$ is the vertical unit vector, $f = 2\Omega\sin\phi$ is the Coriolis parameter with the scalar angular velocity of the Earth Ω, ϕ represents latitude, $\boldsymbol{v}$ is the horizontal velocity field $\boldsymbol{v} = (u, v, 0)$ with the zonal and meridional wind components u and v, $\nabla_p\times$ and ∇_p are the three-dimensional curl and gradient operators applied on levels of constant pressure p, and ∇_θ is the three-dimensional gradient operator applied along levels of constant potential temperature. For adiabatic, frictionless flow, the potential vorticity is conserved following the flow (Ertel 1942; Hoskins *et al.* 1985; Salmon 1998; Gibbon and Holm 2010) which yields a tracer advection equation for q

$$\frac{Dq}{Dt} = 0 \tag{4}$$

$$\Leftrightarrow \frac{\partial q}{\partial t} + \boldsymbol{u} \cdot \nabla q = 0, \tag{5}$$

with D/Dt representing the material derivative and t time. For completeness we note that the flux form of this conservation is given by

$$\frac{\partial(\rho q)}{\partial t} + \nabla \cdot (\boldsymbol{u}\rho q) = 0. \tag{6}$$

As an aside, even diabatic effects like friction (as a general term for all dissipative processes) can be formally included into the PV equations (4) and (6) as e.g. detailed in Haynes and McIntyre (1987, 1990). It yields

$$\frac{Dq}{Dt} = -\frac{1}{\rho}\nabla \cdot \boldsymbol{N} \tag{7}$$

$$\frac{\partial\rho q}{\partial t} + \nabla \cdot (\boldsymbol{u}\rho q + \boldsymbol{N}) = 0 \tag{8}$$

in either Lagrangian or flux form, respectively, where $\boldsymbol{N}$ denotes a nonadvective flux that is driven by e.g subgrid-scale diffusive processes. The exact form of $\boldsymbol{N}$ and how frictional forces enter this vector term is thoroughly discussed in Haynes and McIntyre (1990), but is not relevant here. The important point is that Eqs. (7) and (8) do not contain any source or sink terms in the classical, e.g. chemical, sense. Rather, the diabatic term on the right-hand side of Eq. (7) appears as the specific volume times a divergence and thereby denotes a nonadvective redistribution (transport) process as clearly shown by the flux form in Eq. (8). Such a redistribution is conservative. Therefore, our measure of consistency is also applicable to dynamical cores and tracer advection algorithms in the presence of subgrid-scale dissipation $\boldsymbol{N}$, whether explicitly added or implicitly induced via the numerical scheme. We emphasize that the type of dissipation in the discretized tracer advection algorithm and the dynamical core is most often different. This indicates that the subgrid-scale dissipation may cause inconsistencies between the dynamic PV and its

passive tracer PV counterpart, which is at the very essence of this paper.

Note that there is a substantial body of work on understanding atmospheric dynamics, tracer transport and residence times of chemically and radiatively important trace gases which relies on the correlative relationship of potential vorticity and several tracers (e.g. Newman *et al.* (1988)). One goal of this work is to explore the ability of models to represent the relationship between potential vorticity and tracers, and hence, evaluate the model's ability to represent these important environmental issues and develop strategies to improve the models in this regard. In addition it has been well noted that the reversal of the meridional PV gradient serves as a necessary condition for baroclinic instability as discussed by Charney and Stern (1962), and Hoskins *et al.* (1985) emphasized the invertibility principle of the PV distribution. This further demonstrates the importance of accurately predicting the PV distribution, even beyond the tracer-dynamics consistency arguments in this paper.

From the equations above, the key observation for this paper is that PV is conserved along isentropes that do not intersect the ground. Hence, given initial data denoted by $\boldsymbol{u}_0, \theta_0, \rho_0$ we can define the initial PV field q_0 using Eq. (1) that can be advected via Eq. (4), (5) or (6). The same applies to the hydrostatic PV representations (Eqs. (2) and (3)) provided that $\boldsymbol{v}_0$ and θ_0 are initially known at either pressure or isentropic levels. At any given time t the solution $q(t)$ should be identical to the potential vorticity computed from the dynamical variables $\boldsymbol{u}(t)$, $\theta(t)$ and $\rho(t)$ that are solutions of the dynamical equations of motion (the hydrostatic primitive equations if Eqs. (2) or (3) are used) with initial conditions $\boldsymbol{u}_0, \theta_0, \rho_0$. Therefore, a model that purports to maintain consistency between tracer advection and the integration of the dynamical equations should ensure that a tracer initialized as PV, is identical to PV computed from the dynamic variables. Using PV both as a tracer and a diagnostic computed from the prognostic variables then allows a direct evaluation of a given model's ability to maintain accurate relationships between tracers and dynamic variables.

Such considerations are not entirely new, as Davis *et al.* (1993) compared the evolution of a PV tracer to the diagnostic PV to evaluate the relative effects of latent heating and friction in the evolution of a continental cyclone. Davis *et al.* (1993) use the invertibility principle (see Hoskins *et al.* (1985)) for appropriately balanced flows to then deduce the influence of diabatic processes on the wind and temperature fields. This idea is carried further in Brennan *et al.* (2007) where the non-conservation of PV is used to diagnose the influence of latent heat release on the development of low level jets, and cyclones. The use of a PV tracer is further explored in Stoelinga (1996), Gray (2006), Chagnon and Gray (2009) and Chagnon *et al.* (2013). A detailed explanation of the methodology pursued in these studies is given in Chagnon *et al.* (2013). The essential concept is to introduce a series of tracers into the model evolution that have as sources the calculated diabatic effects of the full (parameterized) model. Each potential diabatic source is assigned to a single tracer which then captures the effects of this source on the transport of the PV. In this way the various potential diabatic sources of PV can be identified and their effects quantified adequately. The goal of the current investigation is to highlight the influence of the underlying numerical scheme on the conservation of PV, completely independent of the diabatic effects explicitly accounted for in the physics parameterizations.

As partial motivation for such a comparison, we note that in the discretized equations the smallest scales are truncated and the scale interaction determined by the nonlinear advective term in the momentum equation cannot be imitated by the linear tracer advection equation. Babiano and Provenzale (2007) and Ohkitani (1991) provide a discussion of this problem for incompressible flows in two dimensions. For three dimensional, fully compressible (even hydrostatic) flow as utilized by most climate models, the passive tracer and dynamical variables are no longer guaranteed to agree once a discrete version of the equations is considered. When certain scales are truncated from the representation of the flow, the inter-scale interaction due to the nonlinear advective term in the momentum equation is not adequately captured, and so the discrete system will no longer maintain consistency, even in the ideal cases of extremely high resolution.

In addition, because the rather coarse typical grid spacings in climate models ($\Delta x \approx 100 - 200$ km in the horizontal directions) do not capture all of the physically relevant dissipation scales, a dissipative mechanism is necessary in GCMs to prevent the build-up of kinetic energy and enstrophy that otherwise could accumulate at the smallest, under-resolved grid scales. Kent *et al.* (2012b) provide a discussion of this with respect to the dynamical cores in CAM which are also used in this study. The dissipative schemes can take the form of filters, explicitly added or implicitly induced numerical diffusion as reviewed in Jablonowski and Williamson (2011). Some of these dissipative mechanisms (particularly linear diffusion) can be well understood, e.g. Whitehead *et al.* (2011) discussed a particular example of an explicitly added diffusion process in CAM-FV. Some nonlinear dissipative processes though, and their impact on the circulation, are harder to assess although one might "hope" that their effects are either negligible or truthfully represent the small-scale, unresolvable features of the flow. Frequently the dynamical core uses a different form of dissipation for the tracer transport algorithm and the dynamical integration. The current investigation is an initial step toward quantifying how these differences affect the dynamical core - tracer consistency.

In this study we use the adiabatic baroclinic wave test case described by Jablonowski and Williamson (2006a), primarily because the analytic initial conditions for the dynamic variables allow us to compute exactly an initial condition for the potential vorticity prescribed as a tracer (tracer PV, see the Appendix). We then follow the tracer during the simulation via Eq. (4), (5) or (6) depending on the model formulation, and compare the tracer's evolution with the computation of the dynamic potential vorticity based on $\boldsymbol{u}, \theta$, and ρ (dynamic PV). In hydrostatic primitive-equation based models only $\boldsymbol{v}$ and θ are needed for the computation of the dynamic PV. We propose several methods for measuring the consistency of a model using the tracer PV and dynamic PV as test fields. The techniques are tested within the CAM 5.1 framework (Neale *et al.* 2010) with its four dynamical cores: CAM-FV, CAM-SE (spectral element), CAM-EUL, and CAM-SLD. We emphasize that the parameter sets and horizontal resolutions we select for each dynamical core are the same used for operational climate simulations, i.e. parameters like the time step or the horizontal diffusion coefficient are chosen to coincide with that used in full-physics model runs to highlight the

consistency of a model at climate resolution. We halved, however, the default CAM 5.1 vertical grid spacing which allows very accurate computations of the dynamic PV field.

This paper is organized as follows. Section 2 briefly surveys the Jablonowski and Williamson (2006a) baroclinic wave test case in the context of comparing the tracer and dynamic PV, before defining some quantitative measures of model consistency. Section 3 provides limited descriptions of the four CAM 5.1 dynamical cores, and describes the results of the PV consistency assessments. Section 4 discusses the possible implications of this work, and includes suggestions for further work. The equations for the analytic tracer PV initialization are included in the Appendix. These results (and particularly the details in the Appendix) are meant to encourage other modelers to utilize the identical setup to examine the consistency of their dynamical cores and tracer advection schemes.

2. Potential Vorticity in an Idealized Setting

2.1. Tracer and dynamic PV in an idealized baroclinic wave

For the current evaluation of model consistency we consider the adiabatic baroclinic wave test case described in Jablonowski and Williamson (2006a,b). This test case starts with an analytically prescribed balanced initial state with an overlaid small-amplitude zonal wind perturbation placed in the northern midlatitudes. A baroclinic wave develops from this perturbation in the Northern Hemisphere after 4 days of integration, breaking around day 9 at low-lying levels. This provides an ideal situation to consider both the development of linear, yet realistic flow prior to the wave breaking, and nonlinear, multi-scale flow afterward.

Figure 1 illustrates the evolution of the dynamic PV field at the interpolated isentropic 300 K and 315 K levels in a CAM-FV $1^\circ \times 1^\circ$ simulation with 60 vertical levels and a model top around 2 hPa. This resolution corresponds to a horizontal grid spacing of about 110 km near the equator. The sloping (with respect to the height or pressure position) 300 K isentropic level depicted in the left column lies around 800-600 hPa in the region between 40°-50°N and intersects the surface at around 30° as indicated in white. The 315 isentropic level lies at about 550-400 hPa in midlatitudes and does not intersect the ground during the life cycle of the wave considered here. Because this level does not intersect the surface, it is relied on heavily for the analysis performed in the following sections.

Figure 1 highlights the progression and the overturning (breaking) of the baroclinic wave during its rapid development phase between days 6-9. The onset of the breaking and the sharpening of the PV gradients are most distinct at low-lying levels around day 9, but are also evident at higher levels at later times. The wave-breaking is graphically identified at the lower level between day 8 and 9 as seen in the left column where the wave starts to fold onto itself. It can also be seen in other fields such as the 850 hPa temperature as displayed in Jablonowski and Williamson (2006a). After the breaking occurs small-scale structures develop. The appearance of small scales from the mean flow indicates that nonlinear effects become dominant in this region (from 90° E to 150° W in longitude). We make the distinction between the linear (prior to wave-breaking at day 8) and nonlinear flow (from day 8 and onward), because the tracer advection algorithm will always be integrating the linear transport equation (4), (5) or (6) for the passive tracer q. The dynamical integration is also effectively integrating the transport equation, but now $q = q(\boldsymbol{u})$ depends on the velocity $\boldsymbol{u}$ and is thereby an active tracer so that the dynamical evolution is nonlinear. This allows additional discretization inconsistencies to occur as discussed above.

We note that the baroclinic wave affects, almost exclusively, a confined latitudinal strip in the Northern Hemisphere over the course of the first 15 days. Therefore, we simplify the comparisons between the dynamic and tracer PV fields, and focus the analyses on the development of the wave in the latitudinal strip between 30° to 90° N (unless specified otherwise). In all our analyses the dynamic PV is first computed along CAM's hybrid η model levels (Simmons and Burridge 1981) before being interpolated to the isentropic 315 K layer. The 315 K level is not close to the domain boundaries in the mid- and high-latitudes and thereby avoids the degradation of the computation due to boundary effects, e.g. the intersection with the surface.

2.2. Quantitative measures of consistency

2.2.1. Paradigms of consistency

There are two basic premises for quantifying the consistency between dynamics and tracer transport of a model. The first premise involves point to point comparisons, i.e. when comparing two data sets it is assumed that both lie on the same grid so that error norms or scatter plots (as explained in the following subsection) can be determined exactly. This is a valid assumption provided the tracer PV and dynamic PV are compared within the same model framework, and at the same resolutions. It is also a viable approach if the dynamic and tracer PV of the same model experiment are vertically interpolated to isentropic levels via an identical algorithm. The second premise is that data on differing grids must be compared, and the influence of the interpolation methods should be minimized. This is of particular interest when the flow is nonlinear, because errors due to interpolations become more significant in complex flow fields with sharp gradients. An accurate computation of the dynamic PV and the choice of the interpolation method from one grid type or resolution are important for PV assessments. This is especially true in the presence of differing vertical discretizations and grids as discussed in Ziv and Alpert (1994).

2.2.2. Point to point comparisons: error norms and scatter plots

A metric used in the analysis of numerical techniques is the discrete l^p norm of the error from an exact solution, i.e., if the model data are represented by q with an exact solution corresponding to q_T, then

$$l^p\{q\} = \left\{ \frac{I\left[(q - q_T)^p\right]}{I\left[(q_T)^p\right]} \right\}^{1/p} \tag{9}$$

defines the normalized l^p error of q where $I[\cdot]$ denotes the area-weighted global integral (in this case, actually the integral over the latitudinal strip from 30° to 90° N at the interpolated isentropic level of 315 K) of the given quantity. The normalized maximum norm $p = \infty$ is

$$l^\infty\{q\} = \frac{\max|q - q_T|}{\max|q_T|}. \tag{10}$$

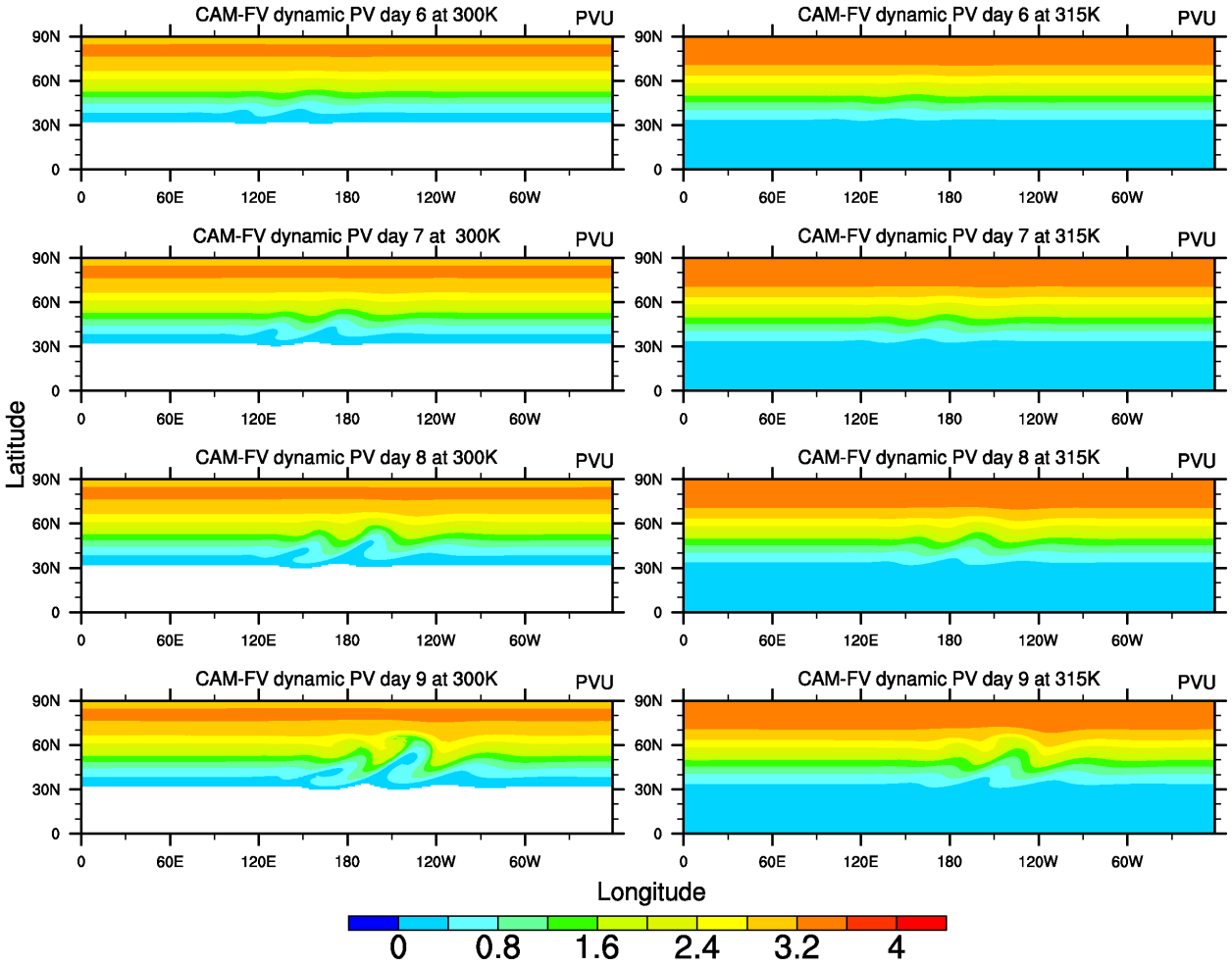

Figure 1. Longitude-latitude cross section of the dynamic potential vorticity in the Northern Hemisphere as simulated with CAM-FV at the horizontal resolution $1^\circ \times 1^\circ$ with 60 levels. The PV evolution at days 6, 7, 8 and 9 at the 300 K isentropic level (left column) and 315 K isentropic level (right column) is shown in potential vorticity units (PVU) defined as PVU= 10^{-6} K m^2 kg^{-1} s^{-1}. The white space at the 300 K isentropic level indicates where the isentrope intersects the earth's surface.

There is no exact solution known for the baroclinic wave test, but the difference between the tracer PV and dynamic PV is a measure of the lack of consistency in the model, i.e. we let q be the tracer PV and q_T the dynamic PV, although this by no means indicates that the dynamic PV is an exact solution. A perfectly consistent model would have identical distributions of tracer PV and dynamic PV. Hence the l^p consistency norm will be due to numerical errors and differences in the integration of the dynamics and the tracer advection algorithm.

Traditionally $p = 2$ (least squares regression) or $p = \infty$ (maximum error norm) are used for measurements of model error. The l^2 error norm does not adequately capture the detrimental effects of extreme differences on small scales, and the maximum error norm l^∞ weighs these statistically rare events more than desired. Hence we choose to consider the l^4 norm (an interpolant between l^2 and l^∞) of the difference between the dynamic and tracer PV. This provides an accurate measure of the overall error as provided by l^2 but includes the effect of localized errors provided by l^∞. If we consider the distribution defined as the pointwise difference between the dynamic and tracer PV, then the l^4 norm gives a measure of the kurtosis of this distribution, indicating the tendency of the differences between dynamics and tracers to originate from localized regions as opposed to a global offset.

The l^4 consistency error norm gives a useful metric for comparing the relative consistency of various models, but it does not indicate the source of these inconsistencies. A qualitative measure related to the consistency error norms are scatter plots such as that illustrated in Fig. 2 (see Zapotocny *et al.* (1996) for the use of similar plots). Each grid point in the domain has both a tracer PV and a dynamic PV value. The horizontal axis of the scatter plot corresponds to the value of the dynamic PV, and the vertical axis is the tracer PV at the same grid point. Ideally the dynamic and tracer PV should agree exactly at all points on the grid, so the scatter plot should follow the line $y = x$ exactly. Deviations from the line $y = x$ then indicate inconsistencies between the dynamic integration and tracer advection algorithm. While it is more difficult to ascertain temporal dependence of inconsistencies with this type of comparison, scatter plots do yield more information than simply calculating the error norm at a given time. For example, as demonstrated schematically in Fig. 2 it appears that for smaller values the tracer PV is larger than the dynamic PV, and the opposite is true for larger values of PV. This gives far more insight into the errors in consistency than the simple calculation of an error norm.

For the current investigation, we construct scatter plots for the tracer PV - dynamic PV comparison for days 1, 8, 12, and 15. The traditional PV unit PVU =10^{-6} K m^2 kg^{-1} s^{-1} is used for both axes. This choice of time-stamps will highlight the inconsistency that arises both from the linear flow up to day 8 (in which case the dynamics and tracer PV should agree very well) and the effects that the nonlinear evolution of the baroclinic wave has on the consistency for days 12 and 15.

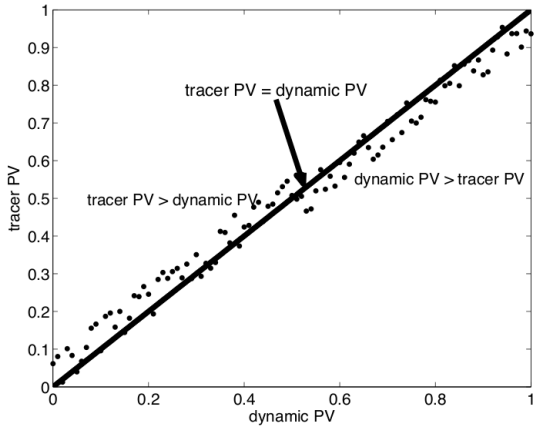

Figure 2: A schematic rendering of a scatter plot comparing dynamic and tracer PV.

2.2.3. *Probability density functions and contour plots*

Theoretically since PV is conserved on closed isentropic surfaces (isentropes that do not intersect the surface of the earth), the probability density function describing the distribution of PV on that surface will not change with time. This provides another useful metric to gauge the conservation/consistency of PV. For the evolution of the baroclinic wave considered in this paper (at least up to day 15), there is little to no exchange of PV across the equator. Assuming such an exchange is negligible, we restrict our attention to the Northern Hemisphere, meaning that a probability density function (pdf) constructed from either the tracer or dynamic PV for each model should not only be the same at any instant of time, but should not evolve with time, i.e. the dynamic and tracer PV pdf should be the same at all times on the selected closed isentropic surface (315 K in the Northern Hemisphere).

For the results of this paper reported in Section 3 we construct a pdf for both the dynamic and tracer PV interpolated to 315 K in the Northern Hemisphere by binning the PV into bins of size β. For the results discussed in Section 3 the bin size is subjectively chosen as $\beta = 0.2$ PVU. Rather than considering the temporal evolution of the dynamic and tracer pdf's for each dynamical core, we consider the difference in these pdf's from the original pdf of the initial state. This indicates the departure of the distribution from what should be a conserved shape, and makes the differences easier to recognize. Recognizing that the distributions in the linear flow regime are nearly identical to the initial state, we only consider these differences in the pdfs at day 15.

Finally, although all of the metrics discussed thus far provide quantitative information with respect to the consistency of a given dynamical core, it is important to also evaluate differences in the fields themselves. In the interest of considering the evolution of the PV only on isentropic surfaces that do not intersect the surface boundary, we look at contour plots of the dynamic and tracer PV at 315 K. Section 3 only displays such a comparison at day 15 as the differences between tracer and dynamic PV are the most stark at this point, although it is instructive to consider the complete temporal evolution of both quantities on this isentrope.

3. Consistency in CAM 5.1

The versatility of CAM's framework is displayed in the work of Rasch *et al.* (2006) wherein three dynamical cores are compared, while using the same physics package. We take a similar approach although we assess the consistency of each of the four dynamical cores in CAM version 5.1 without any physics parameterizations. Each configuration and its parameter set outlined below represents a default which would typically be used at climate resolutions with 100-160 km grid spacing near the equator. We thereby mimic realistic simulations once parameterized physics are included. We make no attempt to match the parameters, like the tracer and dynamics time steps or diffusion mechanisms, from one model to another and note that these are dependent on the numerical schemes, their stability characteristics and the horizontal grid spacings. A detailed parameter sensitivity study, although highly desirable, is beyond the scope of this paper.

3.1. *Model descriptions*

Before examining the results for each of these dynamical cores, we first give a brief description of each. Particular emphasis is placed on the subgrid dissipative mechanisms (filters, diffusion) that are added to each dynamical core. We do not explore every possible form of dissipation or mixing processes in CAM, but consider a few key points that may illustrate differences in the consistency of each model.

3.1.1. *CAM-FV*

The finite volume dynamical core (CAM-FV) and its corresponding tracer transport algorithm are both based on the flux-form semi-Lagrangian scheme of Lin and Rood (1996) on the latitude-longitude grid. The method is a dimensional splitting technique that relies on the one-dimensional finite volume methods akin to the van Leer type monotonic methods (van Leer 1974, 1977) or the Piecewise Parabolic Method (PPM, Colella and Woodward (1984)). The extension of this tracer advection algorithm to the shallow water equations was carried out in Lin and Rood (1997) with further application to three-dimensional hydrostatic motion introduced in Lin (2004). The vertical discretization is based upon a floating Lagrangian approach with periodic remapping to a reference grid. In our study the flow is allowed to freely evolve within the Lagrangian layers for ten dynamics time steps before remapping is invoked.

Implicit diffusion is added to both the dynamics and tracer transport through the nonlinear limiters placed on the underlying one-dimensional finite volume methods. In addition, an explicitly added diffusion mechanism in the form of horizontal divergence damping is implemented in CAM-FV (Whitehead *et al.* 2011). This explicit damping mechanism is present only in the dynamics, there is no analog in the tracer transport for this model, indicating a

possible source of inconsistency. In this paper, the fourth-order horizontal divergence damping mechanism is used. A sponge layer is used to absorb upward traveling waves near the model top to lessen wave reflections. This is applied near the model top in the dynamics using low-order numerics and second-order divergence damping with an increased damping coefficient.

3.1.2. *CAM-EUL*

The spectral-transform Eulerian dynamical core (CAM-EUL) utilizes an underlying quadratic Gaussian transform grid which closely resembles a latitude-longitude mesh. The momentum equations are formulated in vorticity-divergence form. Using spherical harmonics, the prognostic variables are then cast into spectral space and integrated forward in time with a three-time-level leapfrog method. A fourth-order horizontal hyper-diffusion term is added for stability purposes which is applied to the relative vorticity, horizontal divergence and temperature fields. In addition, second-order horizontal diffusion is activated near the model top to mimic a three-layer sponge zone with a base coefficient of 2.5×10^5 m^2 s^{-1}. Additional details on the diffusion and sponge are provided in Jablonowski and Williamson (2011). CAM-EUL uses different methods for the advection of tracers and the evolution of the dynamics. In particular, it employs a monotonic semi-Lagrangian tracer advection scheme that is dimensionally split in the horizontal and vertical directions. Both the interpolations in the semi-Lagrangian scheme and the monotonic constraint are sources of implicit numerical diffusion for the tracers. In addition, the dynamical core and the tracer advection scheme in CAM-EUL invoke a 'mass-fixer' to ensure that conservation of dry air mass and tracer mass is achieved.

3.1.3. *CAM-SLD*

The spectral-transform dynamical core CAM-SLD is based on a semi-Lagrangian approach in both the dynamical core and its tracer advection algorithm, and utilizes the same Gaussian grid as CAM-EUL. However, the semi-Lagrangian interpolations in the tracer advection scheme are monotonic (shape-preserving) whereas they remain unconstrained in the dynamical core. As in CAM-EUL, CAM-SLD is not mass-conserving by design and utilizes a mass fixer. In contrast to CAM-EUL, the tracer transport in SLD is performed in a single three-dimensional step with no dimensional splitting, and SLD utilizes the horizontal velocities u and v as prognostic variables. The time integration is based on a two-time-level semi-Lagrangian semi-implicit time-stepping mechanism. To damp dispersive errors inherent to the spectral-transform spatial discretization, a fourth-order hyper-diffusion term is included in the dynamic calculation, in addition to a second-order diffusive three-layer sponge zone near the model top.

3.1.4. *CAM-SE*

The spectral element (SE) component of CAM (Taylor and Fournier 2010; Taylor 2011) is built on the cubed sphere grid to avoid the singularities generated by a latitude-longitude grid near the poles and increase the scalability on high performance computing platforms (Dennis *et al.* 2005, 2012). CAM-SE utilizes the spectral element approach developed initially for the shallow water equations in Taylor *et al.* (1997) and later expanded to the hydrostatic atmosphere (see Neale *et al.* (2010) for further references). The runs in this paper use a third-order polynomial reconstruction in each element (which is fourth-order accurate). This choice is typical for operational runs. The dynamics and tracer transport are treated similarly in CAM-SE with the tracer transport employing a positivity-preserving limiter which renders the tracer advection scheme third-order accurate. Note however, that the Runge-Kutta time-stepping schemes are slightly different in the dynamical core and the tracer transport scheme, and that different vertical discretizations are used. The CAM-SE dynamical core makes use of a finite-difference scheme in the vertical, whereas CAM-SE's tracer advection scheme utilizes a flow-following Lagrangian coordinate with periodic vertical remapping to a reference grid as in CAM-FV. An explicit fourth-order horizontal hyper-diffusion with identical diffusion coefficients is added to both the dynamics and tracer advection to maintain stability. In addition, the dynamical core applies a second-order horizontal diffusion near the model top to damp the reflection of upward traveling waves.

3.2. *Model comparisons*

Table I details the model configurations for each of the dynamical cores. As noted before the diffusion parameters and time steps are the default values for these resolutions, individually tuned for each dynamical core so that the climate simulations of the full-physics model will yield realistic results. All comparisons are done at climate-type horizontal resolutions which are T85 (triangular truncation) in case of CAM-EUL and CAM-SLD and approximately $1^\circ \times 1^\circ$ in case of CAM-FV and CAM-SE. These resolutions correspond to horizontal grid spacings between 100-160 km near the equator and highlight the effects that unresolved subgrid processes have on the consistency between dynamics and tracers. The T85 and $1^\circ \times 1^\circ$ resolutions can also be considered "equivalent" as determined via aqua-planet studies by Williamson (2008), despite their differences in the number of total grid points. Each model was run with 60 vertical levels (L60). This vertical resolution halves the vertical grid spacings that are typically used in CAM5. The hybrid coefficients for the default 30-level (L30) configuration are listed in Reed and Jablonowski (2012) which enables other modeling groups to use an identical setup. We chose the higher vertical resolution over CAM5's standard 30 levels in order to compute vertical derivatives in the calculation of the dynamic PV more accurately. However, we also conducted L30 experiments (not shown) which led to identical conclusions.

3.2.1. *Point to point comparisons: Error norms, scatter plots and extreme values indicated by contour plots*

A plot of the normalized percentage l^4 error for CAM-FV, CAM-EUL, CAM-SLD, and CAM-SE is shown in Fig. 3 for the model configurations detailed in Table I. The initial differences between the dynamic PV and tracer PV as indicated by the errors at day 0 (left panel of Fig. 3) show that the discrete algorithm for calculating dynamic PV seems to penalize the CAM-SE model relative to the other three dynamical cores. CAM-SE's initial errors are likely due to interpolations of the output from the cubed-sphere to the

Table I. Horizontal model resolutions, time steps Δt for both the dynamics and tracer transport and fourth-order hyper-diffusion coefficients. The triangular truncation T85 is the highest resolved wavenumber in CAM-EUL and CAM-SLD. The CAM-SE resolution $ne30np4$ describes that each cubed-sphere face is divided into 30×30 elements with additional 4×4 collocation points per element to support a third-order polynomial. CAM-FV applies fourth-order divergence damping as explained in Whitehead *et al.* (2011).

Dynamical core	Horizontal resolution	# Horizontal grid points	$\sim$ Grid length at equator	Dynamics Δt (Tracer Δt)	Diffusion coefficient
CAM-FV	$1^\circ \times 1^\circ$	181×360	110 km	180 s (1800 s)	
CAM-EUL	T85	128×256	156 km	600 s (600 s)	1×10^{15} m^{4}s^{-1}
CAM-SLD	T85	128×256	156 km	1800 s (1800 s)	1×10^{15} m^{4}s^{-1}
CAM-SE	$ne30np4$	$6 \times 30 \times 30$ elements	110 km	360 s (1800 s)	1×10^{15} m^{4}s^{-1}

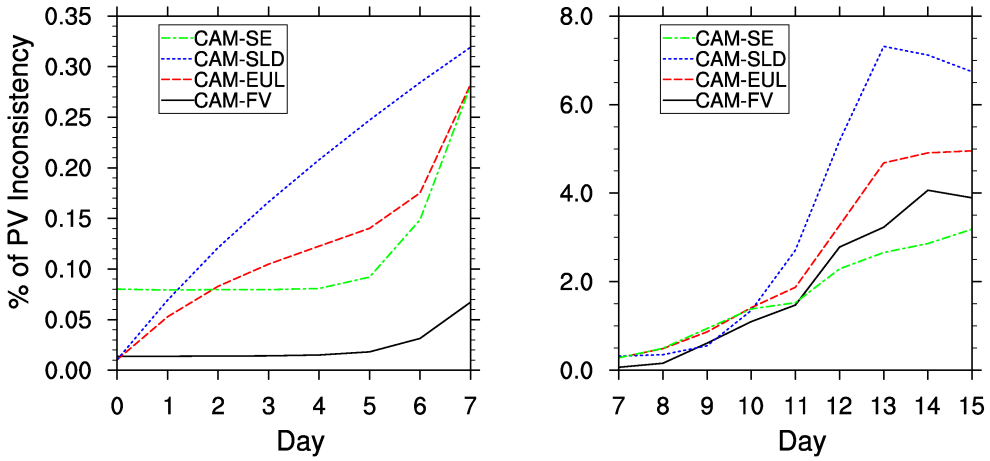

Figure 3. Evolution of the percentage of the nomalized l^4 norm of the difference between dynamic and tracer PV for all four dynamical cores. The left figure shows the linear flow during the first 7 days of the test case, and the right figure shows the evolution of the consistency error during the transition from linear to nonlinear flow (days 7 through 9 approximately), and the evolution of inconsistency for the fully developed nonlinear regime (days 9 through 15). We consider the PV interpolated to 315 K contained in the region between $30^\circ N$ and $90^\circ N$. Note the difference in scale for the vertical axes.

regular latitude-longitude grid (thus simplifying the discrete computation of dynamic PV). Across all four dynamical cores, the maximum initial inconsistency is small and less than 0.1%. Cubic splines were used for the computation of the vertical potential temperature gradient that is part of the PV formulation. A centered finite-difference type method is discouraged for the computation of the potential temperature gradient since it was found to be less accurate.

When the flow is linear with smooth PV distributions at the 315 K isentropic level all four dynamical cores are quite consistent, with consistency errors well below 0.5% even up to day 7 (left panel of Fig. 3). As the flow develops more fully in the right plot, the consistency error worsens, with all four models showing an approximately linear growth in the error until day 11. Around days 11 and 12 though, the spectral-transform models (CAM-EUL and CAM-SLD) demonstrate a significant departure from consistency. As described earlier the spectral-transform dynamical cores are built on similar premises, so the concurrent development of inconsistency at this point may be an indication that the errors are linked to the spectral-transform technique (e.g. occurrence of Gibb's oscillations, generation of small-scale noise or dispersion errors). The dissipative effect of the semi-Lagrangian interpolations in CAM-SLD might have also become more prominent after day 11 as they are triggered by small-scale gradients in the flow field. It is worth noting that CAM-SE outperforms the other three dynamical cores in this measurement of consistency even though the initial inconsistency is worse (at day 0 due to interpolation errors). The better consistency might be a result of CAM-SE's relatively high order, yet local numerical scheme.

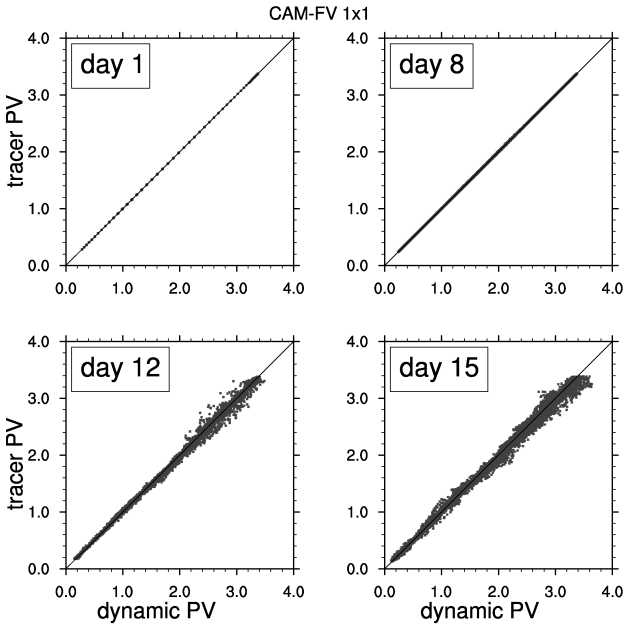

Figure 4: Scatter plots of the tracer and dynamic PV (in PVU) at days 1, 8 (top row), and days 12 and 15 (bottom row) for a CAM-FV $1^\circ \times 1^\circ$L60 simulation in the region 30°-90° N at the 315 K isentropic level. Any deviations from the line $y = x$ indicate differences between tracer PV and dynamic PV.

Scatter plots analyzing the consistency of each dynamical core at days 1, 8, 12, and 15 are shown in Figs. 4, 5, 6, and 7. One feature that is highlighted in all four of these scatter plots is that the tracer PV appears to be bounded by its initial range, i.e. the maximum tracer PV at day 1 is the same as the maximum tracer PV value at day 15. In contrast to the tracer PV, the dynamic PV of CAM-FV, CAM-EUL, and CAM-SLD all have values at day 15 that exceed the initial dynamic PV values. This indicates that the integration of the dynamic PV in these three models is not monotonic, i.e. spurious extrema can be introduced, or physical extrema can be enhanced beyond their physically realistic values. CAM-SE on the other hand, does well in this aspect and appears to retain the same maximal values of dynamic PV that are present at day 1. CAM-SE's preservation of the maximum dynamic PV accounts for some of the better consistency observed in Fig. 3.

Another observation in conjunction with that noted in Fig. 3 is that all four models are very consistent in the linear flow regime, as evidenced by the top two scatter plots in each of Figs. 4- 7. Once the wave breaks and the flow develops into the nonlinear regime the dynamics and tracer separate as evidenced by departures from the line tracer PV = dynamic PV. These inconsistency errors appear to depend on the values of the PV.

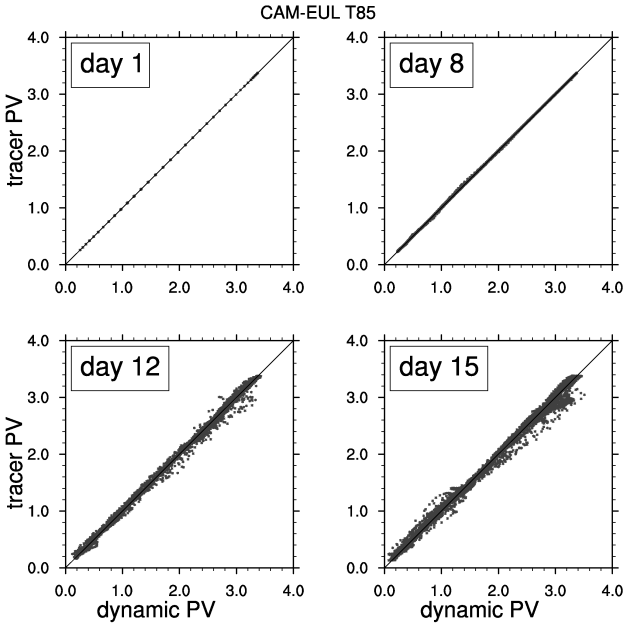

Figure 5: As Fig. 4 but for CAM-EUL T85L60.

At day 12 CAM-FV has developed some spread about the line tracer PV = dynamic PV. Moderate values of the dynamic PV (between 1.5 and 2.0 PVU) generally correspond to equal or lower values of tracer PV. Departures from consistency in the smaller values of PV (less than 1.5 PVU) are less significant and appear to have no preference toward larger values of either the tracer or dynamic PV. Similar statements can be made for the two spectral-transform dynamical cores, where the departures from consistency are more noticeable especially at day 15. In particular, both CAM-EUL and CAM-SLD seem to bias toward large tracer PV for PV less than 1.5 PVU. This same trend is apparent for the very largest PV values (greater than 3.0 PVU) for CAM-EUL. CAM-SLD doesn't exhibit a definitive bias for these largest PV values, but has dynamic PV that has exceeded the initial maximum value of 3.4 PVU. For PV in the moderately high range (from 2.0 to 3.0 PVU) there seems to be a bias toward larger dynamic PV (lies below the line tracer PV = dynamic PV) for the spectral transform models. Although the departures from consistency are not as distinct for CAM-SE, one can see that there is a slight tendency for larger dynamic PV for most of the PV values, with the only significant departure from this observation occurring at the smallest PV values near 0.2 PVU where there is substantially larger tracer PV than dynamic PV.

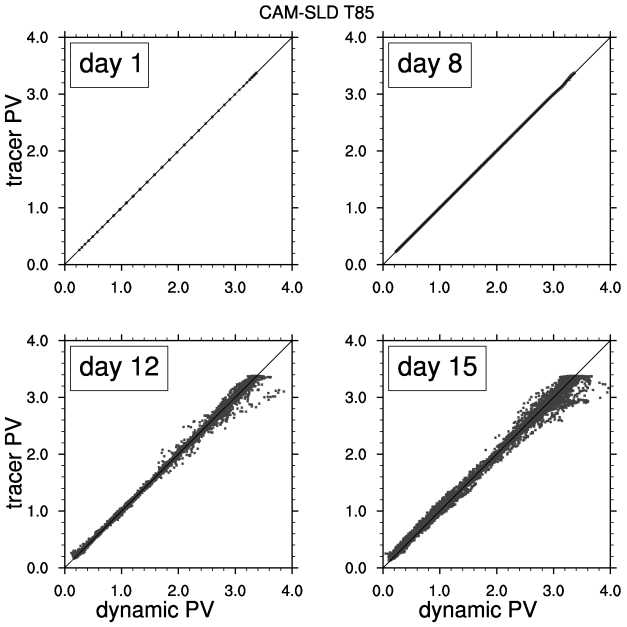

Figure 6: As Fig. 4 but for CAM-SLD T85L60.

In concert with Fig. 3 we note that these scatter plots indicate that CAM-SE is more consistent than the other three models as indicated by how close the scatter plot at day 15 in Fig. 7 is to the line tracer PV = dynamic PV. We suggest that the different biases of each model toward larger dynamic or tracer PV are indicative of the different treatments each model has for the tracer and dynamic integrations. The PV differences in CAM-EUL are most likely due to the numerical inconsistencies between the dynamics and tracer transport scheme. As noted previously the dynamics are treated via a spectral-transform method that may develop dispersive errors that are damped out effectively in the semi-Lagrangian tracer transport used in the same model. Such dispersive errors may also be present in CAM-SLD despite the additional dissipation provided by the (non shape-preserving) semi-Lagrangian interpolations in the CAM-SLD dynamical core. The dissipation in CAM-SE (at least for the model configuration used here) is primarily due to an explicit fourth-order hyper-diffusion for both the dynamics and tracers, indicating a consistent (between dynamics and tracers) treatment of the subgrid scales, leading to less biases in the scatter plots. CAM-FV treats the subgrid scale in the tracer advection algorithm via one-dimensional limiters that preserve monotonicity in the longitudinal and latitudinal directions. The same finite-volume approach is utilized in the dynamical core, but the dimensional splitting can introduce unphysical over- and under-shoots more frequently for the nonlinear part of the flow. This is likely to cause the biases observed for CAM-FV in Fig. 4.

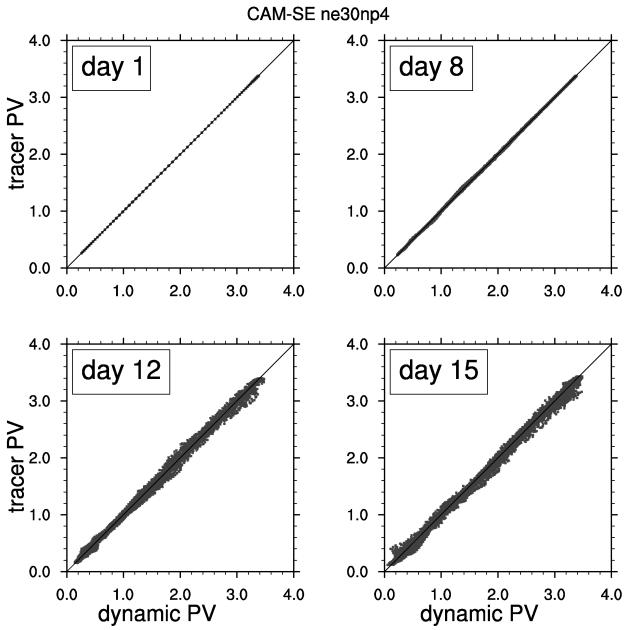

Figure 7: As Fig. 4 but for CAM-SE $ne30np4$ L60.

Figure 8 shows a snapshot of the dynamical and tracer PV at the 315 K isentropic level at day 15, the same day as represented in the bottom right panel of Figures 4-7. We note first that the tracer PV from all of the models are qualitatively similar. For example, between 0 and 60 east and 55 and 80 north, all of the tracer PV plots (RHS of figure), show two distinct orange maxima (2.8-3.2 PVU). Visual examination of the plots shows that fine filaments, for example the green arrows, are present in all simulations. However, filaments in one simulation are not present in the same place as the others. There is no obvious distinction of the tracer PV from one dynamical core to the next. Simulations at different resolutions, not shown, show that the qualitative structure of the highs and lows and filamentation are sensitive to resolution. The similarity of the tracer PV simulations shown here, substantiate the conclusion of Williamson (2008) that we relied on in our choice of equivalent resolutions for the four dynamical cores.

On the left hand side of Figure 8 are the results for the dynamical PV. Looking, again, at 0 and 60 east and 55 80 north, there are discernible differences in the dynamical cores. In all of the dynamical cores there is a maximum exceeding 3.2 PVU. This maximum is not in the tracer PV. In CAM-FV, upper left, there is more small-scale structure in this maximum than in the other dynamical cores. At the location of the red arrow, CAM-FV and CAM-SLD have dynamical PV values which were not present in the initial condition and are, therefore, unphysical under advection. These maxima are likely the source of the large dynamic PV values noted in Figs. 4, 5, 6, and 7.

Note also to the east of the red arrow in CAM-SLD the obvious appearance of rippling. Very close examination of the dynamical PV plots show the emergence of small-scale structures not present in the tracer PV. This is apparent, for example, in between the darker and lighter blues at, approximately, 30 N. At this time CAM-SE has the best agreement of the four dynamical cores tracer PV and dynamic PV.

From these figures we start to see the breakdown of consistency between the tracer PV and the dynamical PV. This appears at scales that are small, and where the dissipative processes in the model are becoming influential. The larger differences are seen in the dynamical PV, where the presence of small-scale structures is amplified in the calculation of the PV. Figure 8 indicates the value of qualitative plots of the potential vorticity, allowing the identification of the spatial structure where inconsistencies occur. This may ultimately provide insight into the interplay between numerical methods and the representation of the physics of mixing in climate models.

3.3. *Probability density functions*

Figure 9 shows the difference between the Northern Hemisphere probability density functions calculated at day 15 and the initial Northern Hemisphere pdf at day 0, for the tracer and dynamic PV of the four dynamical cores considered in this paper. Day 15 is shown to display the effect that the fully nonlinear flow can have on the pdf's. Prior to day 15 the magnitude of the difference values do not exceed 0.02.

The change in the pdfs for the spectral transform dynamical cores has considerably more isolated features (spikes in the Figure) than in the other two dynamical cores. Prior to day 15, the pdfs of CAM-SE and CAM-FV are similar and not as jagged as CAM-EUL and CAM-SLD. The structure of CAM-FV begins to diverge from CAM-SE between days 12 and 15. One feature that all four dynamical cores have is the introduction of a higher probability for PV (both tracer and dynamic) near a PV value of 3.2 PVU. This peak at 3.2 PVU was not present at earlier times, and developed earlier in the spectral transforms dynamical cores. In all dynamical cores the structure at PV values greater than 2.0 increases as the flow becomes nonlinear, after day 9.

For clarification of this feature consider the features present at 75 north and 30 E in Fig. 8. This region has PV of 3.2 PVU. In the dynamical PV the values are higher, and this is where the dynamical PV in CAM-FV is starting to show spatial structure indicative of grid-scale noise. These small-scales activate the implicit dissipative mechanisms in addition to the explicit methods in use. For these high values, the difference of the pdfs for the tracer PV and the dynamical PV increases. This increase is largest in CAM-SE. At day 15 and later, the very values of PV highlighted by the red arrows in Figure 8 start to become more prominent and suggest that the simulation has reached its useful end.

4. Discussion and Summary

We have presented an explicit method for testing the consistency between the representation of dynamical variables and passive tracers in a dynamical core. This was accomplished by including tracer advection of the potential vorticity in the baroclinic wave test case of Jablonowski and Williamson (2006a). This demonstrates the usefulness of potential vorticity as a diagnostic tool in evaluating the consistency between a models dynamics and its tracer transport algorithm.

In the Introduction we documented the need for numerical schemes to be consistent in their representation of transport and mixing of mass, momentum and energy. The simulations presented here suggest a relationship between dissipation and consistency that we expose more fully using the CAM-FV model. A configuration that has extraordinarily good consistency is to run CAM-FV with upwind (first-order) one-dimensional operators for the dynamics (not

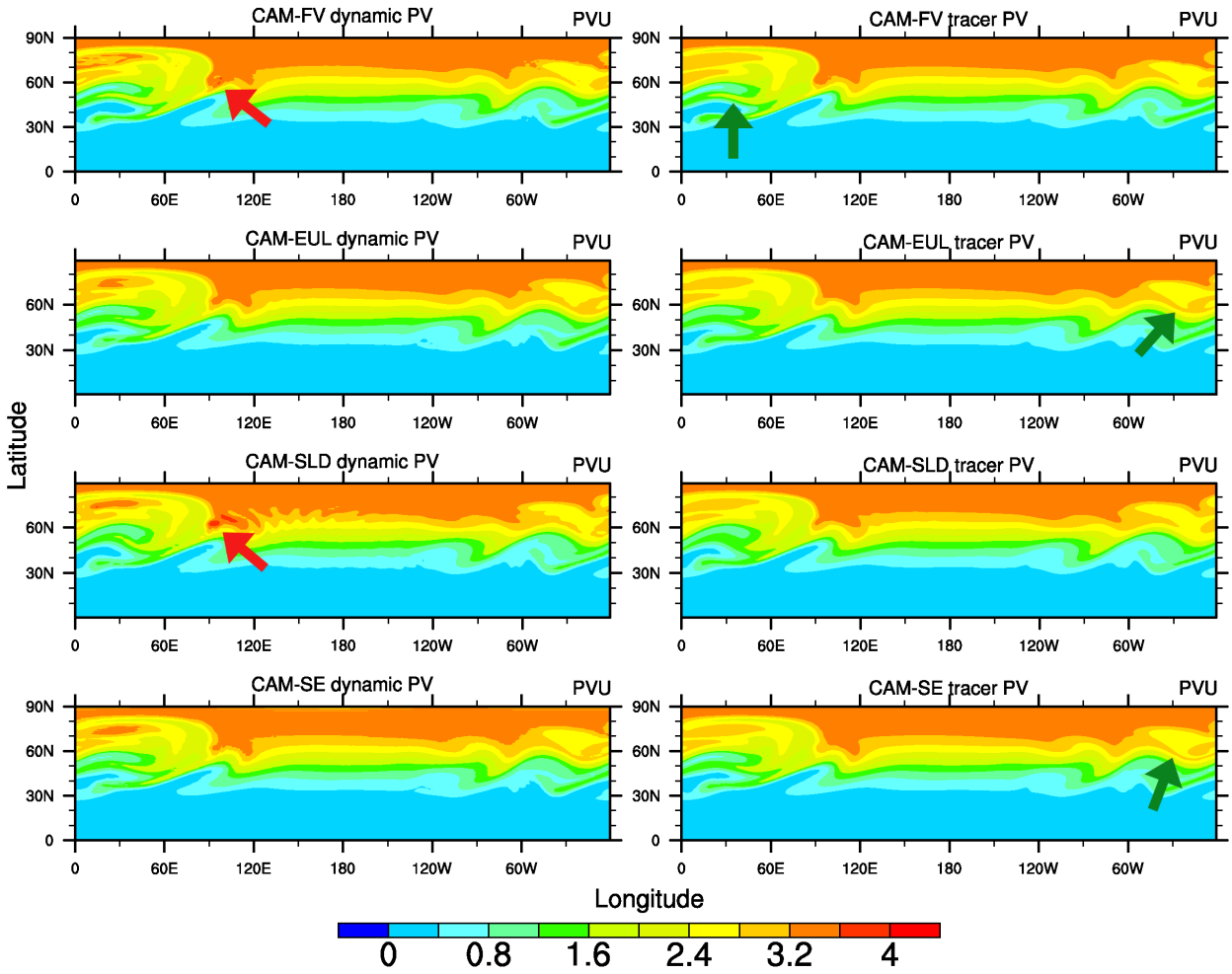

Figure 8. A snapshot at day 15 of the dynamic (left) and tracer (right) PV at the 315 K isentropic level in the Northern Hemisphere for the four dynamical cores to illustrate the differences in their treatment of the dynamics and tracers. The models are run with the configuration described in Table I.

shown). This is extremely dissipative, effectively damping the baroclinic wave so much that the wave does not break until well after day 10, whereupon the nonlinear growth is suppressed so the flow relaxes to a laminar state. This leads to a fundamentally different solution that is quasi-linear, allowing the tracer advection algorithm to perform very well. In this case the consistency of the model for any of the possible tracer algorithms in CAM-FV is very good, but the scheme is highly inaccurate. Throughout these simulations this tension between dissipation, consistency and accuracy are realized.

The results obtained here indicate that CAM-SE is the most consistent of the four dynamical cores in CAM. Simulations are sensitive to resolution, and hence, effort should be taken to assure that the simulations are equivalent in the sense of Williamson (2008) before comparative conclusions are drawn. Simulations of CAM-SE varying the diffusion coefficient in Table I shows that the consistency of CAM-SE is directly related to diffusion, and the default resolution reported here maintains consistency in a balance with accuracy as good as or better than the other schemes. In addition we note that the comparisons, here, indicate that some of the differences observed by Rasch *et al.* (2006) may be explained by the differences in the sub-grid treatment between the different dynamical cores.

The results reported here are for climate resolution studies in which climate-relevant, small-scale features of the nonlinear flow are not fully resolved. We have focused on isentropic surfaces that do not intersect the ground. In all four of the dynamical cores tested in this paper, large inconsistencies develop on isentropes that intersect the surface, as illustrated in Fig. 10 at the low-lying 285 K isentropic level at day 15. The spurious maximum dynamic PV values (called spurious here because they are not present in the tracer PV) that appear where the isentrope intersects the surface (the red regions especially visible from 0 - 160 W and 40 N) are present in all four dynamical cores. They grow in magnitude with increased resolution (not shown). In the simulations reported here, the value of this spurious PV is nearly one order of magnitude larger than the maximum of the tracer PV at the same time stamp and isentropic level. Such PV anomalies are particularly worrisome in the region near 75 N and 20 E where the local minimum of the tracer PV for all the dynamical cores has become a local maximum for the dynamic PV, with the exception of CAM-FV. In addition, significant negative PV appears in these regions indicating a static instability, although this is difficult to visualize as these features are too small. Such PV anomalies near a boundary have been observed previously in reduced models (Nakamura and Held 1989; Garner *et al.* 1992; Schneider *et al.* 2002) and in a full general circulation

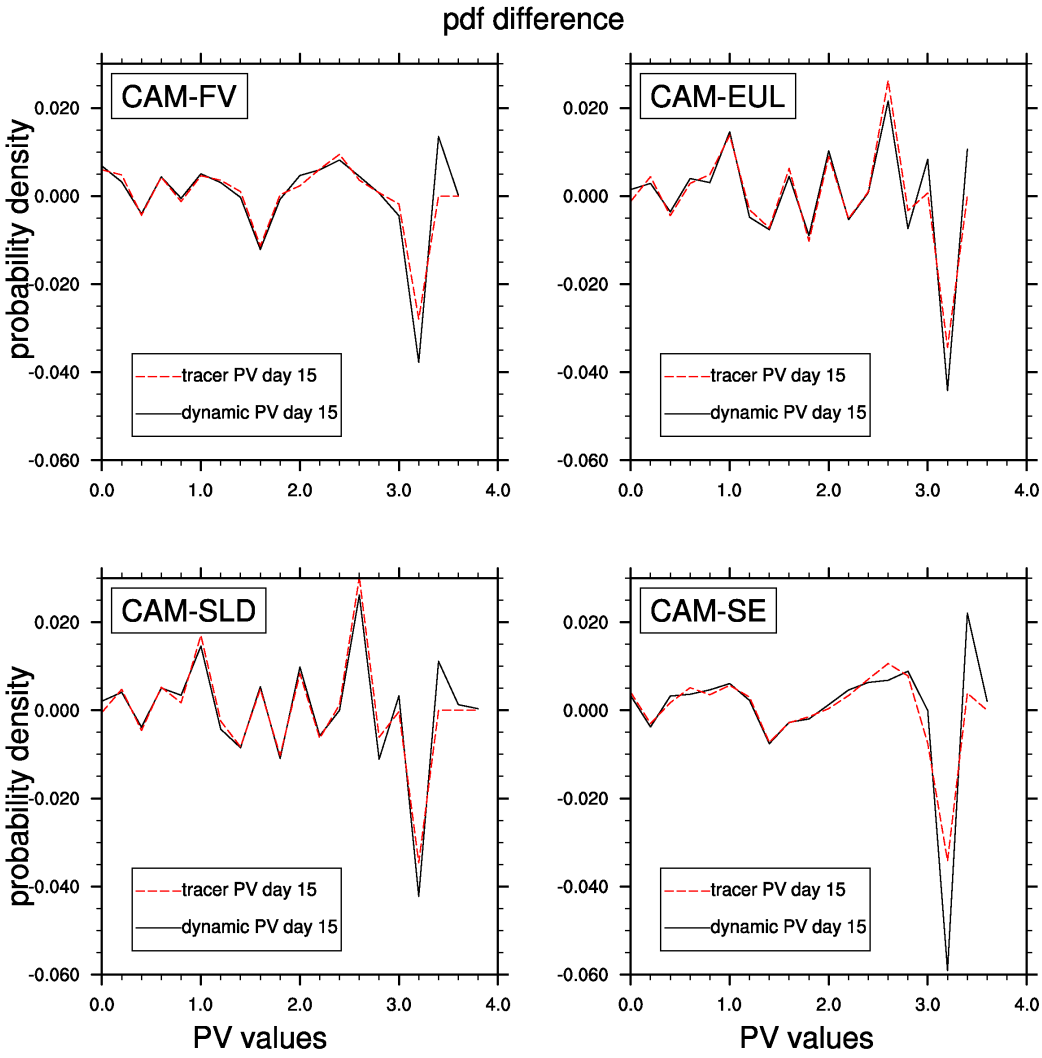

Figure 9. Difference between the Northern Hemisphere probability density functions (pdf) at day 15 with the initial state for the dynamic and tracer PV at 315 K for all four dynamical cores with parameters described in Table I. The horizontal axis is in PVU.

model (Konor and Arakawa 1997; Woolings 2004). In each case, a different driving mechanism for these anomalies is proposed, but there is no consensus as to their source. Using the evaluation technique developed here, we intend to pursue this phenomenon in greater detail.

After the generation of large values of dynamical PV, even prior to the intersection of the isentropic surfaces the ground, the consistency between the dynamic PV and the tracer PV breaks down (Figure 8). This suggests either a numerical artifact or physical phenomena that are not adequately represented in our discrete model. The tracer PV develops neither the large values nor the small-scale structure of the dynamic PV. We draw an analogue to the atmosphere where pdfs and the correlative behavior of PV and tracers have been used to isolate and quantify mixing (Rood *et al.* 1997, 2000). A challenge and a limit of using PV in these applications is that noise is amplified by the derivatives in the PV calculation. The results, here, suggest that there are similar limits even in the calculation of dynamical PV in a relatively simple nonlinear flow. The results also suggest that in climate models carrying a PV-like tracer for diagnostic applications is likely to offer an advantage in determining mixing and the identification of dynamical features.

This point is generalized by considering the importance of the effect of small-scale nonlinear flows on the transport of chemical trace species, specific humidity and cloud liquid water. Ovtchinnikov and Easter (2009) have, for example, argued with respect to cloud-aerosol interactions, that it is important to verify the consistency between the evolution of the winds and the integration of tracers via those winds. Otherwise, the unresolved and under-resolved subgrid-scale effects, that are mimicked by the diffusive processes in the dynamical core, will not be correctly represented in the tracer transport scheme. Such inconsistencies have detrimental effects on the overall simulation quality and affect not just the passive tracers but also cloud schemes and other physical parameterizations through their effect on chemical constituents.

Acknowledgements

We would like to thank two anonymous reviewers and the editors who handled this paper, whose comments greatly enhanced the presentation of this paper, as well as P. H. Lauritzen, C.-Y. Hsu, C. M. Zarzycki, K. A. Reed, P. A. Ullrich and M. A. Taylor for some helpful discussions

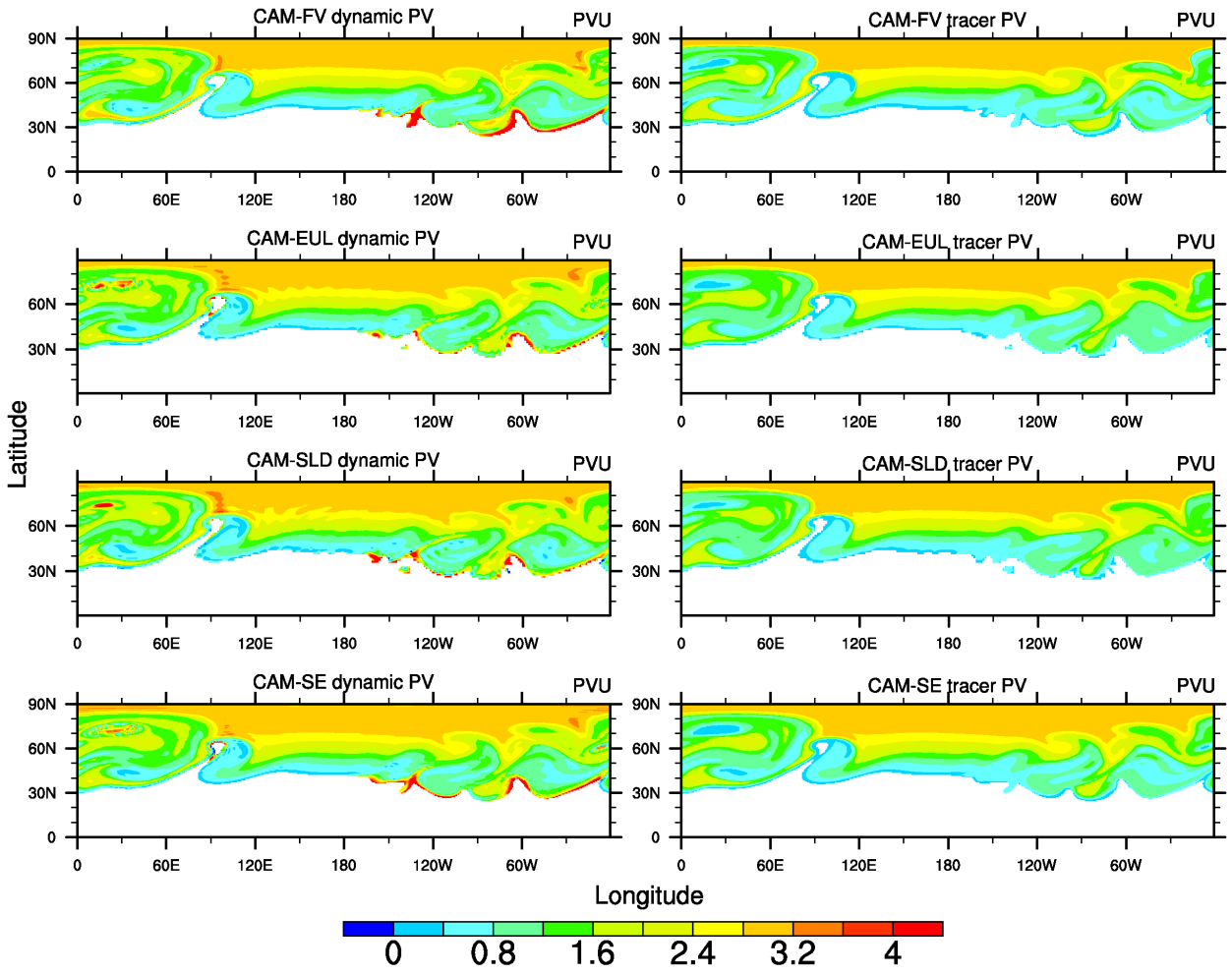

Figure 10. A snapshot at day 15 of the dynamic (left) and tracer (right) PV (in PVU) at the 285 K isentropic level for the four dynamical cores to illustrate the differences in their treatment of the dynamics and tracers. The models are run with the configuration described in Table I. Note that the contours are different than those in Fig. 8. The white space is where the 285 K isentropic level has intersected the surface.

and computational assistance. We acknowledge high performance computing support from the Center for Advanced Computing at the University of Michigan and Yellowstone provided by NCAR's Computational and Information Systems Laboratory, sponsored by the National Science Foundation. This work was supported in part by the U.S. Department of Energy's SciDAC program under grants DE-FG02-07ER64446 and DE-SC0006684, and through the LANL/LDRD Program as well as the National Science Foundation Award DGE-0221611.

Appendix *The Initial Tracer PV*

The expressions for the velocity components, temperature and relative vorticity for the baroclinic wave test case are given in Jablonowski and Williamson (2006a) (their Eqs. (2)-(6) and (12)). Here we only review the new components necessary to analytically compute the initial tracer PV field. The definition of the hydrostatic variant of Ertel's potential vorticity (Hoskins *et al.* 1985) on levels of constant pressure is

$$q = g\left\{\frac{1}{a\cos\phi}\frac{\partial v}{\partial p}\left(\frac{\partial\theta}{\partial\lambda}\right)_p - \frac{1}{a}\frac{\partial u}{\partial p}\left(\frac{\partial\theta}{\partial\phi}\right)_p + (f+\zeta_p)\left(-\frac{\partial\theta}{\partial p}\right)\right\} \tag{11}$$

where a is the Earth's radius, ζ_p the relative vorticity, and λ longitude. The subscript p denotes a constant pressure level. We initialize the tracer with the absolute value of PV ($q = |PV|$) to avoid negative initial PV tracer values in the Southern Hemisphere. Note that the initial potential temperature does not vary in λ, v is zero and that ∂p can be expressed as $p_0\partial\eta$. The underlying relationship $p = \eta p_0$ is only valid under the special condition that the initial surface pressure p_s is equal to the constant reference pressure $p_0 = 1000$ hPa which is the case here. The symbol η denotes the orography-following pressure-based hybrid coordinate (Simmons and Burridge 1981). Using all simplifications in Eq. (11), the initial absolute

value of the PV tracer yields

$$q(\lambda,\phi,\eta) = |\mathrm{PV}(\lambda,\phi,\eta)| = \left| \frac{g}{p_0} \left\{ -\frac{1}{a}\frac{\partial u}{\partial \eta}\left(\frac{\partial \theta}{\partial \phi}\right)_p - (f+\zeta_p)\frac{\partial \theta}{\partial \eta} \right\} \right| \tag{12}$$

To ease the reproducibility of the PV assessments we provide the analytical expressions for the derivative terms in Eq. (12). All symbols and physical constants used below are defined in Jablonowski and Williamson (2006a) and are not all repeated here. The terms are

$$\frac{\partial u}{\partial \eta} = -u_0 \sin^2(2\phi)\frac{3\pi}{4}\cos^{1/2}\eta_v \sin\eta_v \tag{13}$$

$$\frac{\partial \theta}{\partial \eta} = \frac{\partial \overline{\theta}}{\partial \eta} + \frac{3}{4}\frac{\pi u_0}{R_d}\left(1-\frac{R_d}{c_p}\right)\eta^{-R_d/c_p}\sin\eta_v\cos^{1/2}\eta_v Y + \frac{3}{8}\frac{\pi^2 u_0}{R_d}\eta^{1-R_d/c_p}\cos^{3/2}\eta_v Y \tag{14}$$

$$-\frac{3}{16}\frac{\pi^2 u_0}{R_d}\eta^{1-R_d/c_p}\sin^2\eta_v\cos^{-1/2}\eta_v Y \tag{15}$$

$$-\frac{9}{8}\frac{\pi^2 u_0^2}{R_d}\eta^{1-R_d/c_p}\sin^2\eta_v\cos\eta_v\left(-2\sin^6\phi\left[\cos^2\phi+\frac{1}{3}\right]+\frac{10}{63}\right) \tag{16}$$

with $\eta_v = 0.5(\eta-\eta_0)\pi$, $\eta_0 = 0.252$ and

$$Y = \left(-2\sin^6\phi\left[\cos^2\phi+\frac{1}{3}\right]+\frac{10}{63}\right)2u_0\cos^{3/2}\eta_v + \left(\frac{8}{5}\cos^3\phi\left[\sin^2\phi+\frac{2}{3}\right]-\frac{\pi}{4}\right)a\Omega. \tag{17}$$

In addition, the vertical gradient of the potential temperature is given by

$$\frac{\partial \overline{\theta}}{\partial \eta} = \begin{cases} T_0 R_d\left(\frac{\Gamma}{g}-\frac{1}{c_p}\right)\eta^{R_d(\Gamma/g-1/c_p)-1} & \text{for } \eta_s = 1 \geq \eta \geq \eta_t = 0.2 \\ T_0 R_d\left(\frac{\Gamma}{g}-\frac{1}{c_p}\right)\eta^{R_d(\Gamma/g-1/c_p)-1} & \text{for } \eta_t > \eta \\ -\Delta T\left(5(\eta_t-\eta)^4\eta^{-R_d/c_p}+\frac{R_d}{c_p}(\eta_t-\eta)^5\eta^{-R_d/c_p-1}\right) & \end{cases}.$$

The derivative of the potential temperature with respect to the latitudinal direction on a constant pressure level is given by

$$\left(\frac{\partial \theta}{\partial \phi}\right)_p = \frac{3}{4}\frac{\pi u_0}{R_d}\eta^{1-R_d/c_p}\sin\eta_v\cos^{1/2}\eta_v \tag{18}$$

$$\times\left\{2u_0\cos^{3/2}\eta_v\left(-12\cos\phi\sin^5\phi\left[\cos^2\phi+\frac{1}{3}\right]+4\cos\phi\sin^7\phi\right)\right. \tag{19}$$

$$\left. + a\Omega\left(-\frac{24}{5}\sin\phi\cos^2\phi\left[\sin^2\phi+\frac{2}{3}\right]+\frac{16}{5}\cos^4\phi\sin\phi\right)\right\}. \tag{20}$$

The appendix of Jablonowski and Williamson (2006a) outlines how the initial conditions can be computed for models with height-based vertical coordinates, if needed. This analytic tracer PV initialization is also valid for non-hydrostatic dynamical cores that utilize the shallow-atmosphere approximation.

References

Babiano A, Provenzale A. 2007. Coherent vortices and tracer cascades in two-dimensional turbulence. *Journal of Fluid Mechanics* **574**: 429–448.

Brennan MJ, Lackmann GM, Mahoney KM. 2007. Potential Vorticity (PV) thinking in operations: The utility of nonconservation. *Weather and Forecasting* **23**: 168–182.

Chagnon JM, Gray SL. 2009. Horizontal potential vorticity dipoles on the convective storm scale. *Quarterly Journal of the Royal Meteorological Society* **135**: 1392–1408.

Chagnon JM, Gray SL, Methven J. 2013. Diabatic processes modifying potential vorticity in a north atlantic cyclone. *Quarterly Journal of the Royal Meteorological Society* **139**: 1270–1282.

Charney JG, Stern ME. 1962. On the stability of internal baroclinic jets in a rotating atmosphere. *Journal of the Atmospheric Sciences* **19**: 159–172.

Colella P, Woodward PR. 1984. The Piecewise Parabolic Method (PPM) for gas-dynamical simulations. *Journal of Computational Physics* **54**: 174–201.

Davis CA, Stoelinga MT, Kuo YH. 1993. The integrated effect of condensation in numerical simulations of extratropical cyclogenesis. *Monthly Weather Review* **121**: 2309–2330.

Dennis JM, Edwards J, Evans KJ, Guba O, Lauritzen PH, Mirin AA, St-Cyr A, Taylor MA, Worley PH. 2012. CAM-SE: A scalable spectral element dynamical core for the Community Atmosphere Model. *International Journal of High Performance Computing Applications* **26**(1): 74–89.

Dennis JM, Fournier A, Spotz WF, St-Cyr A, Taylor MA, Thomas SJ, Tufo H. 2005. High-resolution mesh convergence properties and parallel efficiency of a spectral element atmospheric dynamical core. *International Journal of High Performance Computing Applications* **19**(3): 225–235.

Ertel H. 1942. Ein neuer hydrodynamischer Wirbelsatz. *Meteorologische Zeitschrift* **59**: 271–281.

Garner ST, Nakamura N, Held IM. 1992. Nonlinear equilibrium of two-dimensional Eady waves: A new perspective. *Journal of the Atmospheric Sciences* **49**(21): 1984–1996.

Gibbon JD, Holm DD. 2010. Stretching & folding diagnostics in solutions of the three-dimensional Euler & Navier-Stokes equations. *arXiv* (1012.359v1).

Gray SL. 2006. Mechanisms of midlatitude cross-tropopause transport using a potential vorticity budget approach. *Journal of Geophysical Research* **111**.

Haynes PH, McIntyre ME. 1987. On the evolution of vorticity and potential vorticity in the presence of diabatic heating and frictional or other forces. *Journal of the Atmospheric Sciences* **44**(5): 828–841.

Haynes PH, McIntyre ME. 1990. On the conservation and impermeability theorems for potential vorticity. *Monthly Weather Review* **47**(16): 2021–2031.

Hoskins BJ, McIntyre ME, Robertson AW. 1985. On the use and significance of isentropic potential vorticity maps. *Quarterly Journal of the Royal Meteorological Society* **111**: 877–946.

Jablonowski C, Williamson DL. 2006a. A baroclinic instability test case for atmospheric model dynamical cores. *Quarterly Journal of the Royal Meteorological Society* **132**(621): 2943–2975.

Jablonowski C, Williamson DL. 2006b. A baroclinic wave test case for dynamical cores of General Circulation Models: Model intercomparisons. NCAR Tech. Note NCAR/TN-469+STR, National Center for Atmospheric Research, Boulder, Colorado. 89 pp.

Jablonowski C, Williamson DL. 2011. The pros and cons of diffusion, filters, and fixers in atmospheric general circulation models. In: *Numerical Techniques for Global Atmospheric Models, Lecture Notes in Science and Engineering*, vol. 80, Lauritzen PH, Jablonowski C, Taylor MA, Nair RD (eds), Springer, pp. 381–493.

Joeckel P, von Kuhlmann R, Lawrence MG, Steil B, Brenninkmeijer CAM, Crutzen PJ, Rasch PJ, Eaton B. 2001. On a fundamental problem in implementing flux-form advection schemes for tracer transport in 3-dimensional general circulation and chemistry transport models. *Quarterly Journal of the Royal Meteorological Society* **127**: 1035–1052.

Kent J, Jablonowski C, Whitehead JP, Rood RB. 2012a. Assessing Tracer Transport Algorithms and the Impact of Vertical Resolution in a Finite-Volume Dynamical Core. *Monthly Weather Review* **140**: 1620–1638.

Kent J, Jablonowski C, Whitehead JP, Rood RB. 2012b. Downscale cascades in tracer-transport test cases: An intercomparison of the dynamical cores in the Community Atmosphere Model CAM5. *Geoscientific Model Development* **5**: 1517–1530.

Konor CS, Arakawa A. 1997. Design of an atmospheric model based on a generalized vertical coordinate. *Monthly Weather Review* **125**(7): 1649–1673.

Lamarque JF, Kinnison DE, Hess PG, Vitt FM. 2008. Simulated lower stratospheric trends between 1970 and 2005: Identifying the role of climate and composition changes. *Journal of Geophysical Research* **113**: 1–19.

Lauritzen PH, Ullrich PA, Nair RD. 2011. Atmospheric transport schemes: Desirable properties and a semi-Lagrangian view on finite-volume discretizations. In: *Numerical Techniques for Global Atmospheric Models, Lecture Notes in Science and Engineering*, vol. 80, Lauritzen PH, Jablonowski C, Taylor MA, Nair RD (eds), Springer, pp. 187–248.

Lee SM, Yoon SC, Byun DW. 2004. The effect of mass inconsistency of the meteorological field generated by a common meteorological model on air quality modeling. *Atmospheric Environment.* **38**(18): 2917–2926.

Lin SJ. 2004. A "vertically Lagrangian" finite-volume dynamical core for global models. *Monthly Weather Review* **132**: 2293–2307.

Lin SJ, Rood RB. 1996. Multidimensional flux-form semi-Lagrangian transport scheme. *Monthly Weather Review* **124**: 2046–2070.

Lin SJ, Rood RB. 1997. An explicit flux-form semi-Lagrangian shallow water model on the sphere. *Quarterly Journal of the Royal Meteorological Society* **123**: 2477–2498.

Nair RD, Lauritzen PH. 2010. A class of deformational flow test-cases for linear transport problems on the sphere. *Journal of Computational Physics* **229**: 8868–8887.

Nakamura N, Held IM. 1989. Nonlinear equilibration of two-dimensional Eady waves. *Journal of the Atmospheric Sciences* **46**(19): 3055–3064.

Neale RB, Chen CC, Gettelman A, Lauritzen PH, Park S, Williamson DL, Conley AJ, Garcia R, Kinnison D, Lamarque JF, Marsh D, Mills M, Smith AK, Tilmes S, Vitt F, Cameron-Smith P, Collins WD, Iacono MJ, Easter RC, Liu X, Ghan SJ, Rasch PJ, Taylor MA. 2010. Description of the NCAR Community Atmosphere Model (CAM 5.0). NCAR Technical Note NCAR/TN-486+STR, National Center for Atmospheric Research, Boulder, Colorado, pp. 268.

Newman PA, Schoeberl MR, Plumb RA, Rosenfield JE. 1988. Mixing rates calculated from potential vorticity. *Journal of Geophysical Research* **93**: 5221–5240.

Ohkitani K. 1991. Wave number space dynamics of enstrophy cascade in a forced 2-dimensional turbulence. *Physics of Fluids A* **3**: 1598–1611.

Ovtchinnikov M, Easter RC. 2009. Nonlinear advection algorithms applied to interrelated tracer: Errors and implications for modeling aerosol-cloud interactions. *Monthly Weather Review* **137**: 632–644.

Rasch PJ, Coleman DB, Mahowald N, Williamson DL, Lin SJ, Boville BA, Hess P. 2006. Characteristics of atmospheric transport using three numerical formulations for atmospheric dynamics in a single GCM framework. *Journal of Climate* **19**: 2243–2266.

Reed KA, Jablonowski C. 2012. Idealized tropical cyclone simulations of intermediate complexity: a test case for AGCMs. *Journal of Advances in Modeling Earth Systems* **4**: M04 001.

Rood RB. 2011. A perspective on the role of the dynamical core in the development of weather and climate models. In: *Numerical Techniques for Global Atmospheric Models, Lecture Notes in Science and Engineering*, vol. 80,

Lauritzen PH, Jablonowski C, Taylor MA, Nair RD (eds), Springer, pp. 523–544.

Rood RB, Douglass AR, Cerniglia MC, Read WG. 1997. Synoptic-scale mass exchange from the troposphere to the stratosphere. *Journal of Geophysical Research* **102**(D19): 23 467–23 485.

Rood RB, Douglass AR, Cerniglia MC, Sparling LC, Nielsen JE. 2000. Seasonal variability of middle-latitude ozone in the lowermost stratosphere derived from probability distribution functions. *Journal of Geophysical Research* **105**(D14): 17 793–17 805.

Salmon R. 1998. *Lectures on geophysical fluid dynamics*. Oxford University Press. 378 pp.

Schneider T, Held IM, Garner ST. 2002. Boundary effects in potential vorticity dynamics. *Journal of the Atmospheric Sciences* **60**: 1024–1040.

Simmons AJ, Burridge DM. 1981. An energy and angular-momentum conserving vertical finite-difference scheme and hybrid vertical coordinate. *Monthly Weather Review* **109**: 758–766.

Stoelinga MT. 1996. A potential vorticity-based study of the role of diabatic heating and friction in a numerically simulated baroclinic cyclone. *Monthly Weather Review* **124**: 849–874.

Taylor MA. 2011. Conservation of mass and energy for the moist atmospheric primitive equations on unstructured grids. In: *Numerical Techniques for Global Atmospheric Models*, *Lecture Notes in Science and Engineering*, vol. 80, Lauritzen PH, Jablonowski C, Taylor MA, Nair RD (eds), Springer, pp. 357–380.

Taylor MA, Fournier A. 2010. A compatible and conservative spectral element method on unstructured grids. *Journal of Computational Physics* **229**: 5879–5895.

Taylor MA, Tribbia J, Iskandarani M. 1997. The spectral element method for the shallow water equations on the sphere. *Journal of Computational Physics* **130**: 92–108.

van Leer B. 1974. Towards the ultimate conservative difference scheme, II. Monotonicity and conservation combined in a second order scheme. *Journal of Computational Physics* **14**: 361–370.

van Leer B. 1977. Towards the ultimate conservative difference scheme, III. Upstream centered finite-difference schemes for ideal compressible flow. *Journal of Computational Physics* **23**: 263–275.

Wan H, Wang B, Yu YQ, Yu RC. 2006. Development and validation of the grid point atmospheric model of IAP LASG (GAMIL). Technical Report 16, LASG, Institute of Atmospheric Physics, Chinese Academy of Sciences.

Wang B, Wan H, Li ZZ, Zhang X, Yu RC, Yu YQ, Liu HT. 2004. Design of a new dynamical core for global atmospheric models based on some efficient numerical methods. *Science in China (A)* **47 (Suppl.)**: 4–21.

Whitehead JP, Jablonowski C, Rood RB, Lauritzen PH. 2011. A stability analysis of divergence damping on a latitude-longitude grid. *Monthly Weather Review* **139**(9): 2976–2993.

Williamson DL. 2007. The evolution of dynamical cores for global atmospheric models. *Journal of the Meteorological Society of Japan* **85B**: 241–269.

Williamson DL. 2008. Equivalent finite volume and Eulerian spectral transform horizontal resolutions established from aqua-planet simulations. *Tellus Series A* **60**: 839–847.

Woolings T. 2004. Entropy and potential vorticity in dynamical core atmosphere models. PhD thesis, University of Reading. 201 pp.

Zapotocny TH, Lenzen AJ, Johnson DR, Reames FM, Poitowicz PA, Schaak TK. 1996. Joint distributions of potential vorticity and inert trace constituent in CCM2 and UW $\theta - \sigma$ model simulations. *Geophysical Research Letters* **23**(18): 2525–2528.

Zhang K, Wan H, Wang B, Zhang M. 2008. Consistency problem with tracer advection in the atmospheric model GAMIL. *Advances in Atmospheric Science* **25**(2): 306–318.

Ziv B, Alpert P. 1994. Isobaric to isentropic interpolation errors and implication to potential vorticity analysis. *Journal of Applied Meteorology* **33**: 694–703.